DEM-LBM simulation of stress-dependent absolute and relative permeabilities in porous media

Citation for published version:
Huang, J, Xiao, F, Labra, C, Sun, J & Yin, X 2021, 'DEM-LBM simulation of stress-dependent absolute and relative permeabilities in porous media', *Chemical Engineering Science*, vol. 239, pp. 116633. https://doi.org/10.1016/j.ces.2021.116633

Digital Object Identifier (DOI):
10.1016/j.ces.2021.116633

DEM-LBM Simulation of Stress-dependent Absolute and Relative Permeabilities in Porous Media

Jingwei Huang[1,2*], Feng Xiao[2], Carlos Labra[3], Jin Sun[3] and Xiaolong Yin[2*]

1. Department of Petroleum Engineering, Texas A&M University

2. Department of Petroleum Engineering, Colorado School of Mines

3. School of Engineering, University of Edinburgh

Abstract

In this work, stress-dependent absolute and relative permeabilites in porous media are studied using the discrete element method and lattice Boltzmann method. The change of absolute permeability and porosity during compaction is found follow a power-law relation. The stress-dependent absolute permeability in homogeneous pack is in agreement with the prediction of Carman-Kozeny equation. Porosity exponent is increased due to the existence of vugs but is decreased with fractures. Relative permeability, on the other hand, is found not only affected by pore structure of compacted media, but also properties of fluids and rock surface. Our simulations indicate that relative permeability of wetting phase increases slightly with increasing stress, due to the formation of more continuous pathways. Relative permeability of non-wetting phase, however, either increases or decreases depending on viscosity ratio and capillary number. It is found that lubrication effects play an important role in the stress sensitivity of relative permeability.

Keywords: Stress sensitivity, absolute/relative permeability, DEM-LBM, lubrication effects

1. Introduction

In subsurface environment, rocks are continuously under the influences of overburden, confining, and pore pressures. The state of stress in these rocks evolves gradually during geological time. Rapid changes in stress can be induced by engineering activities such as withdrawal and replenishment of aquifers [1, 2], primary production of petroleum [3, 4], injection of fluids during CO_2 sequestration [5, 6] and enhanced oil recovery [7, 8]. Pore shape and pore size are altered by the change of stress, which results in changes in macroscopic porosity, absolute permeability and relative permeability of the rock that are central to the rate of flows. Stress sensitivity of intrinsic rock properties is therefore essential to accurately model the single- and multi-phase flow at subsurface.

Absolute permeability and porosity of rocks vary in a wide range, depending on rock types and effective stress [9]. Reduction in porosity and absolute permeability by compaction has been well documented in the literature [3, 10]. Both linear and nonlinear relations have been observed between absolute permeability/porosity and strain in different porous media [11-14]. When changed absolute permeability is correlated to changed porosity, a particularly simple correlation is a power-law

$$\left(\frac{\phi}{\phi_0}\right)^A = \frac{k}{k_0} \tag{1}$$

where ϕ_0 and k_0 are the porosity and permeability at a reference state, respectively, and ϕ and k are changed porosity and permeability at another stress state. A is a material constant named the porosity-sensitivity exponent. The value of A in the literature varies [15-18], depending on type of rock and range/history of applied stress [19]. Heterogeneity of rocks also has great impact on A. Experimental results showed that A in fractured rocks are higher than those in carbonates, which in turn are higher than those in sandstones [20]. It was pointed out that pore throats are more stress sensitive than pore bodies, which would lead to larger values of A [21]. Similarly, as conductive fractures are more stress sensitive than pores in rock's matrix, fractured rocks also exhibit larger values of A [20].

Compared to absolute permeability, fewer attempts have been made to study stress sensitivity of relative permeability, and findings reported in the literature have significant variability. For gas-liquid flows, some experiments showed for sandstones that the relative permeability of gas was not affected by changed overburden pressures [22, 23]. Zhang et al. [24] found for coal that the relative permeability of gas increased and that of water decreased when the confining pressure was increased. Experiments from Haghi et al. [25] showed for sandstone, however, that the relative permeability of water increased but that of nitrogen decreased under increased confining stress. Experiments conducted on water-oil systems also generated variable results. Some researchers reported that relative permeability of water slightly increased or did not change while that of oil decreased under increased stress [26-30]. However, experiments of Wilson [31] indicated that relative permeability of water decreased and that of oil increased when the overburden pressure was increased. Hamoud et al. [32] found that stress sensitivity of relative permeability depends on the range of strain. Their experiments showed that relative permeability of water increased when strain was less than 2% but decreased when strain was within 2%-15%. Relative permeability of oil increased when strain was less than 5% but decreased when strain was within 5%-15%. Al-Quraishi et al. [33] investigated changes in relative permeabilities of sandstones under different conditions of loading. They found that relative permeability of water increased and that of oil decreased when the axial stress was increased at fixed confining pressure. Opposite trends were observed for the relative permeabilities of both phases when the confining pressure was increased at fixed axial stress. Table 1 summarizes the experimental studies to date on stress sensitivity of relative permeabilities including types of rocks, properties of fluids and rock surface, and conditions of stress employed.

Apartment from experiments, some pore-scale numerical simulations have also been conducted to study the behavior of relative permeability under stress. Fagbemi et al. [34] simulated drainage and imbibition in a digital sandstone medium under quasi-static triaxial loading. Deformation of rock was solved using a finite element method and multiphase flow was modeled using a volume of fluid method. They found the relative permeability of non-wetting phase (oil) decreased when stress loading was increased and explained it as due to the reduction in the cross-sections of oil's pathways. The relative permeability of water was not significantly affected. In another study from the same authors [35], the same methods were applied and relative permeabilities of both wetting and non-wetting phases decreased with increasing stress. Fan et al. [36] studied the relative permeability in a proppant-packed hydraulic fracture under compaction. They found that the relative permeability of oil increased first and then decreased when the effective stress was increased continuously. The relative permeability of water was less sensitive to the stress.

The behavior of relative permeability with stress is highly variable because, unlike absolute permeability that only depends on the structure and connectivity of pores, relative permeability is affected by other factors such as wettability, viscosity ratio and capillary number. In the absence of compaction, it was shown that the relative permeability of water increased when pore surface became more oil-wet [37]. The relative permeability of the non-wetting phase increased with increasing viscosity ratio between the non-wetting phase and the wetting phase. The relative permeability of the wetting phase, on the other hand, was less sensitive to viscosity ratio [38, 39]. On the effect of capillary number, Li et al. [39] and Ramstad et al. [40] both found that relative permeabilities of wetting and non-wetting phases increased with increasing capillary number. The above studies indicate that when compaction changes the geometry of pores, its effect on relative permeability should also depend on the state of wettability, viscosity ratio and capillary number. Existing experiments and simulations on stress sensitivity of relative permeability however have not evaluated these conditions comprehensively.

Pore-scale, direct numerical simulation of two-phase flow is an effective approach to obtain relative permeability of porous media under controlled conditions, and the lattice Boltzmann method is a particularly simple and efficient numerical tool. Various multiphase lattice Boltzmann models have been developed, such as the color-gradient model [41-43], pseudo-potential model [44, 45], free energy model [46] and mean-field model [47]. They all have been successfully applied to investigate multiphase flow problems such as co-current flows with viscosity contrast [39], imbibition and drainage in porous media [48], and multiphase flows with mixed wettability [49]. Relative permeability has been calculated for both synthetic media [48] and digitalized rocks [40, 50].

In this study, we aim to comprehensively evaluate the stress sensitivity of absolute and relative permeability in a simple porous medium made by spherical particles. A sphere pack can be regarded as a standard representation of unconsolidated porous media [14]. Deformations of sphere pack under isotropic and uniaxial loading conditions were modeled by using discrete element method (DEM). In this work, only small and linearly elastic deformations were modeled. Single- and multiphase flows through original and deformed sphere packs at different stages of loading were simulated by the lattice Boltzmann method (LBM). The rest of the paper is organized as follows. We first present methods of DEM and LBM applied in this study. Then, original porosities and absolute permeabilities of sphere packs and changes in them due to stress are presented for both homogeneous and heterogeneous sphere packs. Finally, relative permeabilities are calculated at different stages of loading for the homogeneous pack, with varied fluid properties and wetting conditions.

Table 1: Summary of experimental results on the stress sensitivity of relative permeability.

Authors (dates)	**Fluids**	**Porous medium**	**Wettability**	**Viscosity**	**Stress condition**	**Conclusions**
Fatt, 1953	Gas-oil	Sandstone	Not reported	Not reported	Overburden pressure	Relative permeability of gas was not affected under 3000 Psi.
Tomas and Ward, 1972	Gas-water	Sandstone	Not reported	Not reported	Overburden pressure	Relative permeability of gas was not significantly affected under 6000 Psi.
Zhang et al. 2017	Gas-water	Coal	Not reported	Not reported	Confining pressure	Relative permeability of water decreased; Relative permeability of gas increased.
Haghi et al. 2019	Nitrogen-water	Sandstone	Not reported	Water: 0.6527 cp Nitrogen: 0.184 cp	Confining pressure	Relative permeability of water increased; Relative permeability of nitrogen decreased.
Wilson, 1956	Brine-oil	Sandstone	Water wet	Oil: 1.7-2.7 cp Brine: not reported	Overburden pressure	Relative permeability of brine decreased; Relative permeability of oil increased.
Ali et al. 1987	Water-oil	Sandstone	Water wet	Not reported	Overburden pressure	Relative permeability of water was not significantly affected; Relative permeability of oil decreased.
Jones et al. 2001	Brine-oil	Sandstone	Strongly water-wet	Oil: 1.33 cp Brine: 1.31 cp	Overburden pressure	Relative permeability of water slightly increased; Relative permeability of oil decreased.
Al-Quraishi and Khairy 2005	Brine-oil	Sandstone	Water wet	Oil: 7.1 cp Brine: 0.98 cp	Overburden pressure	Relative permeability of water lightly increased; Relative permeability of oil decreased.
Gawish and Al-Homadhi 2008	Brine-oil	Sandstone	Water wet	Oil: not reported Brine: 1.06 cp	Overburden pressure	Relative permeability of water was not significantly affected; Relative permeability of oil decreased.
Al-Quraishi et al. 2010	Water-oil	Sandstone	Strongly water-wet	Oil: 18 cp Water: 1 cp	Confining pressure or axial stress	Relative permeability of water increased and that of oil decreased when increasing the axial stress at fixed confining pressure. An opposite trend was found when increasing the confining pressure at fixed axial stress.
Hamoud et al. 2012	Water-oil	Sandstone	Water wet	Not reported	Triaxial compression	Relative permeability of water increased within 0%-2% strain but decreased within 2%-15%; Relative permeability of oil increased within 0%-5% strain but decreased within 5%-15%.
Adenutsi et al. 2019	Water-oil	Artificial core samples	Water wet	Oil: 1.48 cp Water: 0.89 cp	Confining pressure	Relative permeability of water slightly increased; Relative permeability of oil decreased.

2. Numerical Methods

In this section, we briefly explain the numerical methods used in this study. As introduced, DEM was employed to solve the deformation of porous media. A single-phase LB model was used for calculation of absolute permeability and a color-gradient LB model was applied to simulate multiphase flows for characterization of relative permeability.

2.1 Discrete element method

Discrete element method (DEM) with bonded particle model has been widely applied to simulate deformation of granular media, such as rocks [51, 52], soil [53, 54] and porous ceramics [55]. In DEM, a material is represented by a collection of interacting particles with idealized shape, e.g., sphere in 3D and disk in 2D. The equations of particle motion can be described by the Newton and the Euler equations

$$m_i \ddot{\boldsymbol{u}}_{\boldsymbol{i}} = \mathbf{F}_{\boldsymbol{i}} \tag{2}$$

$$I_i \dot{\boldsymbol{\omega}}_{\boldsymbol{i}} = \mathbf{T}_{\boldsymbol{i}} \tag{3}$$

where m_i, $\boldsymbol{u}_{\boldsymbol{i}}$, I_i and $\boldsymbol{\omega}_{\boldsymbol{i}}$ are the mass, displacement, moment of inertia and angular velocity of the *i*th particle respectively. $\mathbf{F}_{\boldsymbol{i}}$ the force and $\mathbf{T}_{\boldsymbol{i}}$ the moment acting on the particle are sums of all forces and moments applied to the particle

$$\mathbf{F_i} = \mathbf{F_i^{ext}} + \sum_{c=1}^{n_c} \mathbf{F_i^c} + \mathbf{F_i^{damp}} \tag{4}$$

$$\mathbf{T_i} = \mathbf{T_i^{ext}} + \sum_{c=1}^{n_c} (\mathbf{r_i^c} \times \mathbf{F_i^c}) + \mathbf{T_i^{damp}} \tag{5}$$

where $\mathbf{F}_{\boldsymbol{i}}^{\boldsymbol{ext}}$ and $\mathbf{T}_{\boldsymbol{i}}^{\boldsymbol{ext}}$ are external load, n_c is the number of particles in contact with the *i*th particle, $\boldsymbol{r}_{\boldsymbol{i}}^{\boldsymbol{c}}$ is the vector connecting the center of the *i*th particle with the point of contact **c**, $\mathbf{F}_{\boldsymbol{i}}^{\boldsymbol{c}}$ is contact interaction force. $\mathbf{F}_{\boldsymbol{i}}^{\boldsymbol{damp}}$ and $\mathbf{T}_{\boldsymbol{i}}^{\boldsymbol{damp}}$ are force and moment resulted from external damping. When damping is non-viscous, they are given by

$$\mathbf{F}_{\boldsymbol{i}}^{\boldsymbol{damp}} = -\alpha^t \left\| \mathbf{F}_{\boldsymbol{i}}^{\boldsymbol{ext}} + \sum_{c=1}^{n_c} \mathbf{F}_{\boldsymbol{i}}^{\boldsymbol{c}} \right\| \frac{\dot{\boldsymbol{u}}_i}{\|\dot{\boldsymbol{u}}_i\|} \tag{6}$$

$$\mathbf{T}_{\boldsymbol{i}}^{\boldsymbol{damp}} = -\alpha^r \left\| \mathbf{T}_{\boldsymbol{i}}^{\boldsymbol{ext}} + \sum_{c=1}^{n_c} (\boldsymbol{r}_{\boldsymbol{i}}^{\boldsymbol{c}} \times \mathbf{F}_{\boldsymbol{i}}^{\boldsymbol{c}}) \right\| \frac{\dot{\boldsymbol{\omega}}_i}{\|\dot{\boldsymbol{\omega}}_i\|} \tag{7}$$

where α^t and α^r are damping constants for transitional and rotational motions, respectively. Contact laws that include force and moment interactions between particles determine the behavior of the system. The contact force can be decomposed into normal component $\mathbf{F}_{\boldsymbol{i,n}}^{\boldsymbol{c}}$ and tangential component $\mathbf{F}_{\boldsymbol{i,t}}^{\boldsymbol{c}}$

$$\mathbf{F}_{\boldsymbol{i}}^{\boldsymbol{c}} = \mathbf{F}_{\boldsymbol{i,n}}^{\boldsymbol{c}} + \mathbf{F}_{\boldsymbol{i,t}}^{\boldsymbol{c}} \tag{8}$$

In the present work, an elastic–perfectly brittle model [56] is used. The contact interface is characterized by normal stiffness k_n and tangential stiffness k_t

$$\mathbf{F}_{\boldsymbol{i,n}}^{\boldsymbol{c}} = k_n \boldsymbol{u}_{\boldsymbol{rn}} \tag{9}$$

$$\mathbf{F}_{\boldsymbol{i,t}}^{\boldsymbol{c}} = k_t \boldsymbol{u}_{\boldsymbol{rt}} \tag{10}$$

where $\boldsymbol{u}_{\boldsymbol{rn}}$ and $\boldsymbol{u}_{\boldsymbol{rt}}$ are normal and tangential relative displacements, respectively. The tangential force is constrained by the Coulomb friction law

$$\|\mathbf{F}_t\| \leq \mu |f_n| \tag{11}$$

where μ is the friction coefficient. Bonds between particles are broken instantaneously when normal or tangential forces exceed their respective bond-strength constraints. For detailed information of applied DEM model, the readers are referred to Labra et al. [54].

2.2 Lattice Boltzmann method

Absolute and relative permeabilities of sphere packs before and after deformation were calculated by three-dimensional lattice Boltzmann flow simulators [48, 57]. LBM is a well-established computational fluid dynamic (CFD) method. Since it handles no-slip boundary using a simple bounce-back scheme, it is a particularly popular method for modelling fluid flows in media with complex geometries [57, 58]. LBM solves the Navier-Stokes equation indirectly by simulating the evolution of velocity distribution function, the moments of which give macroscopic density and velocity of the flow. When using MRT (multi-relaxation time) collision operator, the transport equation for the velocity distribution function is

$$f_i(\boldsymbol{x}+\boldsymbol{c}_i\Delta t, t+\Delta t) = f_i(\boldsymbol{x},t) - \mathbf{M}^{-1}\cdot\mathbf{S}\cdot\mathbf{M}\cdot\left[f_i(\boldsymbol{x},t) - f_i^{eq}\right] \tag{12}$$

where $f_i(\boldsymbol{x},t)$ is the distribution function at position $\boldsymbol{x}$ and time t, f_i^{eq} is the equilibrium distribution function. $\Delta t = 1$ is the time step and i represents propagation direction corresponding to lattice velocity $\boldsymbol{c}_i$. $\mathbf{M}$ is an integer transformation tensor and $\mathbf{S}$ is diagonal collision matrix [59, 60]. For two-phase flows, simulations used a color gradient model [48]. In this model, f_i^R and f_i^B are used to represent the velocity distribution functions of two immiscible fluids (red and blue). The evolution equation can be written as

$$f_i^k(\boldsymbol{x}+\boldsymbol{c}_i\Delta t, t+\Delta t) = f_i^k(\boldsymbol{x},t) + \Omega_i^k(\boldsymbol{x},t) \tag{13}$$

In Eqn. (13), $f_i^k(\boldsymbol{x},t)$ is the distribution function of fluid k ($k = R$ or B). Ω_i^k is the collision operator that includes three parts:

$$\Omega_i^k = \left(\Omega_i^k\right)^3\left[\left(\Omega_i^k\right)^1 + \left(\Omega_i^k\right)^2\right] \tag{14}$$

where $\left(\Omega_i^k\right)^1$ is the single-phase collision operator

$$\left(\Omega_i^k\right)^1 = -(\boldsymbol{M}^{-1}\boldsymbol{S}\boldsymbol{M})_{ij}[f_j - f_j^{eq}] \tag{15}$$

in which f_j is the total distribution function $f_j = f_j^R + f_j^B$ and f_j^{eq} is the equilibrium distribution of total distribution function. $\left(\Omega_i^k\right)^2$ is the two-phase collision operator

$$\left(\Omega_i^k\right)^2 = \frac{A}{2}|\nabla\rho^N|\left[\omega_i\frac{\left(\boldsymbol{c}_i.\nabla\rho^N\right)^2}{|\nabla\rho^N|^2} - B_i\right] \tag{16}$$

where ω_i and B_i are weighting coefficients, A is a parameter that controls interfacial tension σ that can be determined through static drop simulations. ρ^N is a phase field function defined as

$$\rho^N(\boldsymbol{x},t) = \frac{\rho_R(\boldsymbol{x},t)-\rho_B(\boldsymbol{x},t)}{\rho_R(\boldsymbol{x},t)+\rho_B(\boldsymbol{x},t)} \tag{17}$$

where ρ_R and ρ_B are densities of the red and the blue fluids, respectively. $\left(\Omega_i^k\right)^3$ is the recoloring operator that forces phase separation

$$(\Omega_i^R)^3(f_i^R) = \frac{\rho_R}{\rho} f_i + \beta \frac{\rho_R \rho_B}{\rho^2} cos(\varphi_i) f_i^{eq}(\rho, 0) \tag{18}$$

$$(\Omega_i^B)^3(f_i^B) = \frac{\rho_B}{\rho} f_i - \beta \frac{\rho_R \rho_B}{\rho^2} cos(\varphi_i) f_i^{eq}(\rho, 0) \tag{19}$$

where ρ is total density ($\rho = \rho_R + \rho_B$), β is a free parameter controls interface thickness, and φ_i is the angle between the gradient of the phase field $\nabla\rho^N$ and $\boldsymbol{c}_i$.

As to boundary conditions, the link-bounce-back scheme of Frisch et al. [61] was used to recover the no-slip boundary condition on fluid-solid surfaces. To implement wettability, it was assumed that the solid wall is a mixture of two fluids with a certain value of ρ^N [49, 62]. For instance, if the contact angle of red fluid is θ, ρ^N should be set as $\cos\theta$. For detailed information of applied two-phase LB models, the readers are referred to Huang et al. [48].

3. Numerical Results and Discussions

In this section, we first introduce the porous medium built by spherical particles. The changes in porosity and absolute permeability by compaction were then studied in both homogeneous and heterogeneous sphere packs. Both hydrostatic and uniaxial loading were investigated. In the end, relative permeabilities of homogeneous packs were calculated for both loading conditions, with effects of wettability, viscosity ratio and capillary number evaluated.

3.1 Sphere packs under stress

To study the effect of stress on permeability, a porous medium made up by spherical particles was built using a dense packing algorithm [63]. As shown in Figure 1(a), the porous medium consists of 25,277 spherical particles filling a cubic domain of 9 cm × 9 cm × 9 cm, bounded by six flat solid walls (not shown). The distribution of particle size is Gaussian, shown in Figure 1(b). The smallest and the largest particles have diameters of 1.34 mm and 6.64 mm, respectively. Number-averaged particle diameter is 3.71 mm. The initial net porosity of the medium is 0.2281.

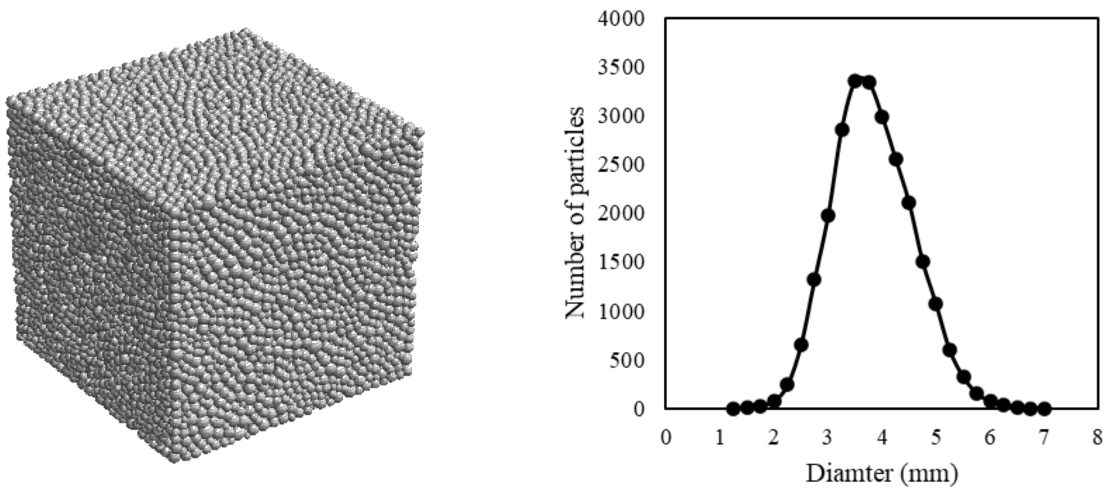

(a) (b)

Figure 1. Porous medium built by the dense packing algorithm (a) and distribution of particle size (b).

DEM was then applied to model compaction of the medium under stress. Parameters of particle-particle interactions in DEM and resulted bulk mechanical properties of the medium are listed in Table 2. Both hydrostatic loading and uniaxial loading were tested, as illustrated in Figure 2. These loadings were implemented by moving the bounding walls. In uniaxial loading, only the walls bounding the y direction of the medium were moved and those bounding x and z directions were fixed. In hydrostatic loading, all three pairs of walls were moved. Three stages of strain were simulated for each condition of loading, and the maximum strain reached at the third stage is about 2%. Figure 3 presents the reduction in porosity of the medium with strain. Porosity is normalized by its initial value (0.2281) before loading. In hydrostatic loading, porosity was decreased by 11.5% at the maximum strain. In uniaxial loading, maximum reduction in porosity was about 5.4%. Porosity of the medium decreased linearly with strain under the hydrostatic loading condition. For uniaxial loading the trend is slightly nonlinear.

Table 2. Particle-particle interaction model parameters for DEM and porous medium bulk mechanical properties [20].

Particle normal stiffness (MN/m)	60.37
Particle tangential stiffness (MN/m)	11.47
Particle friction coefficient	0.5
Bond normal strength (kN)	2.81
Bond tangential strength (kN)	1.12
Young's modulus (GPa)	18.7
Poisson's ratio	0.21
Compressive strength (GPa)	1.27
Tensile strength (GPa)	0.12

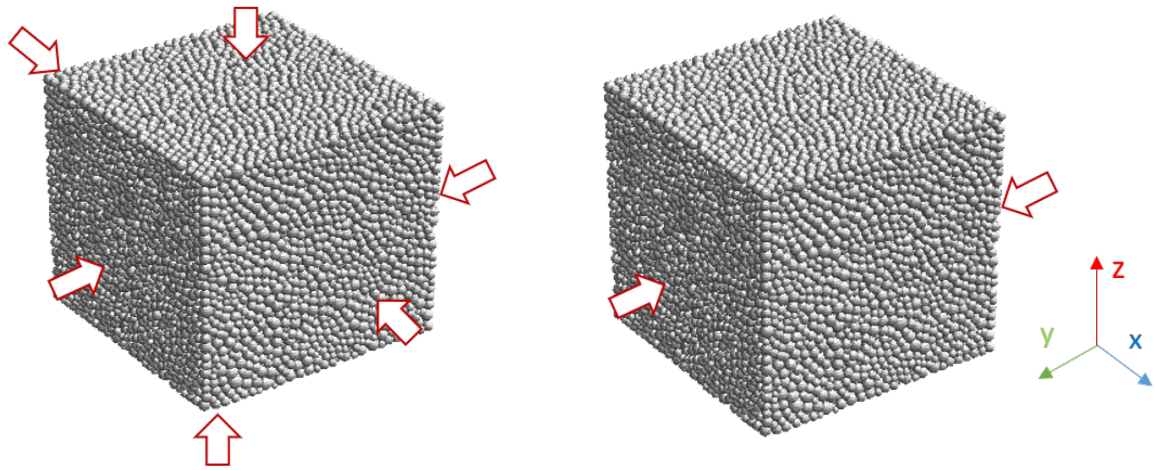

(a) (b)

Figure 2. Porous medium under hydrostatic loading (a) and uniaxial loading (b).

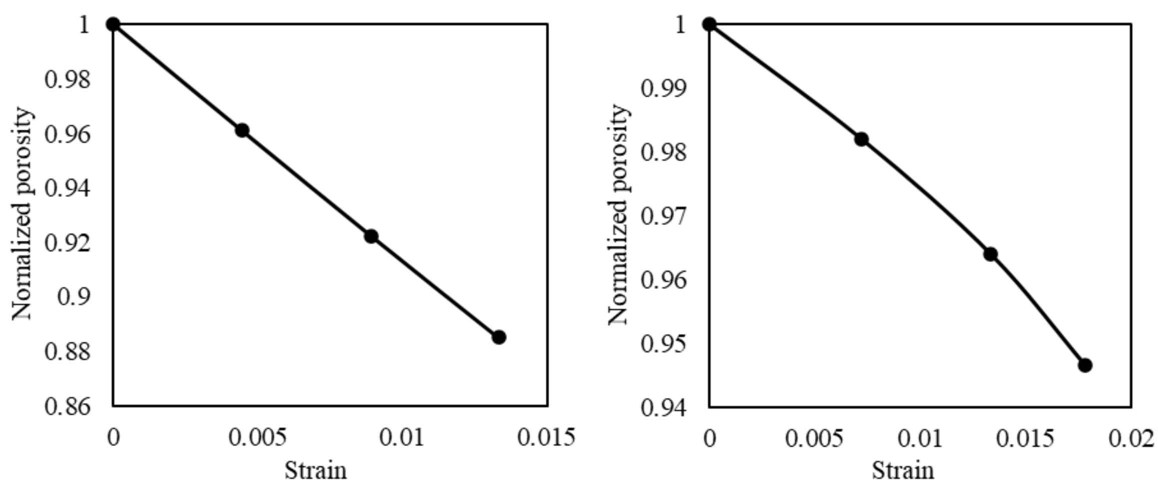

(a) (b)

Figure 3. Relations between porosities of porous medium and external strains during hydrostatic loading (a) and uniaxial loading (b).

3.2 Absolute permeability under stress

In this section, we present stress sensitivity of absolute permeability. Fluid flow was simulated by using a single-phase LBM. A constant external body force $F = 1 \times 10^{-5}$ was used to drive the flows. The viscosity of fluid is 0.1667 by setting relaxation time as one. When MRT collision operator is applied, calculated permeability is independent of relaxation time [39, 48]. The Mach number of the system was in the magnitude of 10^{-7}. After flows became steady, absolute permeabilities of the medium before and after compaction were calculated by Darcy's law, using viscosity of the fluid, body force, and the steady superficial velocity of the fluid through the medium.

The medium before compaction was resolved by a $N \times N \times N$ cubic lattice. It is known that resolution can affect calculated permeability [39]. Thus, a convergence test was first conducted by setting N to 250, 375, 500, and 1000. Errors of calculated absolute permeabilities along x direction of the original medium are presented in Figure 4. These errors are defined as $|k_N - k_{1000}|/k_{1000}$, where k_N is the absolute permeability using resolution N. Figure 4 shows that the relative error between the case with $N = 500$ and that with $N = 1000$ is within 4%. To save computational time, a 500^3 computational domain was used to resolve the medium. When $N = 500$, the size of a voxel is 180^3 μm^3. Under this resolution, spheres are resolved by 21 voxels in average along their diameters and the smallest sphere is resolved by 7 voxels. Compacted media were resolved at the same resolution, i.e. 180^3 μm^3. Lattices for compacted media were therefore slightly shorter than the original N^3 lattice along the direction of compaction, by about ten lattices at the maximum strain of 2%. We note that, since in DEM compaction of the medium was achieved by movement of the confining walls, there are ordered, high-porosity zones near the walls where particles are excluded. These zones, if not excluded from simulations, would create high-permeability pathways and affect absolute permeabilities. To exclude these zones from simulations, a 400^3 sub-domain in the center of the larger domain was used in the flow simulations. Periodic boundary conditions were applied on all sides of simulated domain.

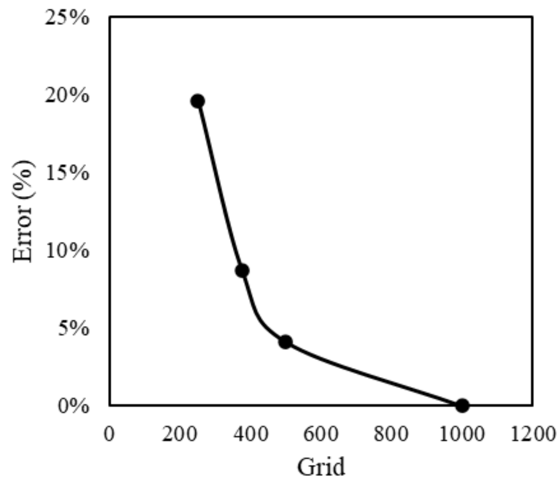

Figure 4. Effect of grid resolution on convergence of the absolute permeability of the original medium.

Absolute permeabilities of compacted media in three directions are presented in Figure 5 as functions of strain. These absolute permeabilities are normalized using the original permeabilities of the medium before compaction, which are very close to each other due to the isotropy of the medium: $1.52 \times 10^{-9}\, m^2$, $1.53 \times 10^{-9}\, m^2$, and ,$1.54 \times 10^{-9}\, m^2$ in x, y, and z directions, respectively. Figure 5 shows that the absolute permeability is reduced by 34% at the maximum strain under the hydrostatic loading condition. In the case of uniaxial loading, the maximum reduction of absolute permeability is 14% in the direction of applied stress (y direction) and 19% in the lateral directions (x and z directions). Similar to the changes in porosity in Section 3.1, absolute permeability decreased linearly under the hydrostatic loading condition and nonlinearly under the uniaxial loading condition in all directions. Changed porosity and permeability during compaction follow the power-law relation in Eqn. (1). Figure 6 shows that linear relations were present between $log_{10}(k/k_0)$ and $log_{10}(\phi/\phi_0)$ in all directions. The slopes of the lines gave porosity exponents A, summarized in Table 3.

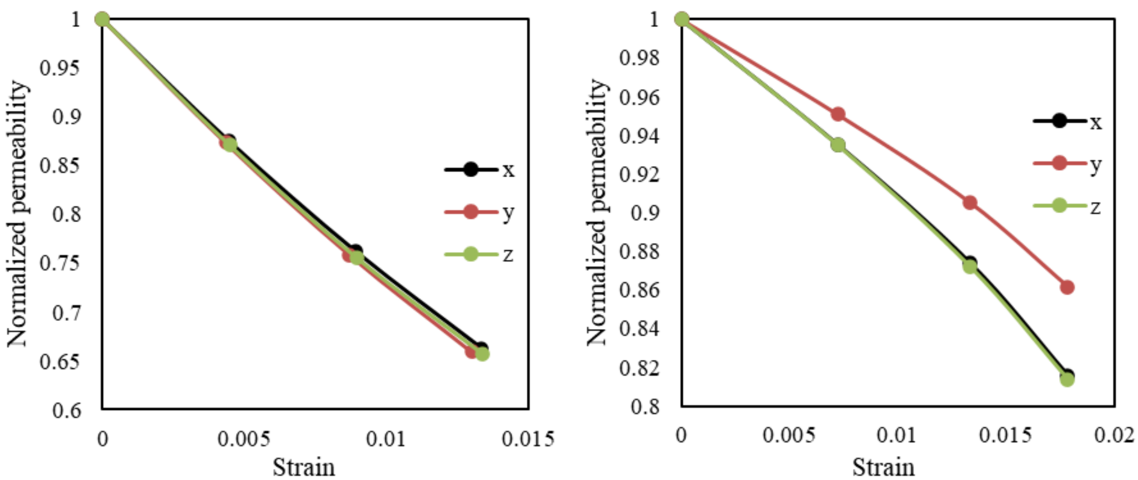

(a) (b)

Figure 5. Relations between absolute permeabilities of porous medium and external strains under hydrostatic loading (a) and uniaxial loading (b).

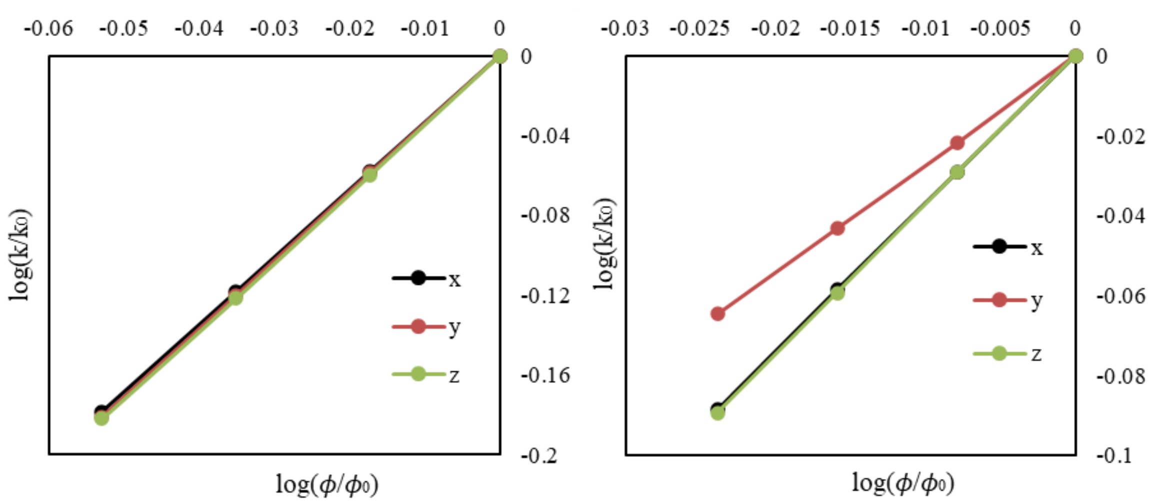

(a) (b)

Figure 6. Changes in porosity correlated to changes in permeability under the hydrostatic loading condition (a) and the uniaxial loading condition (b).

Table 3. Porosity exponents of homogeneous sphere pack

Hydrostatic loading			Uniaxial loading		
A_x	A_y	A_z	A_x	A_y	A_z
3.4	3.5	3.5	3.8	2.8	3.8

We note that according to the Carman-Kozeny equation

$$k = \frac{\phi^3(1-\phi)^2}{C\tau^2 S^2} \tag{20}$$

where τ is the tortuosity, C is a constant and S is the surface area of connected pores per unit solid volume, A should take the value of three if tortuosity, surface area and solid volume are nearly independent of stress and changes in ϕ and k are small relative to ϕ_0 and k_0. Under the hydrostatic loading condition, A_x, A_y, A_z are nearly identical due to the isotropy of the medium and that of the applied stress. Moreover, all of them are close to the theoretical value of three from the Carman-Kozeny equation. Under the uniaxial loading condition, A_x and A_z are identical as expected, and they are both larger than A_y, which indicates that this loading condition generated anisotropy in the absolute permeability, and those along the lateral directions (x and z direction) are more sensitive to porosity compaction.

In a previous experimental study [19], porosity and permeability changes in sandstones, carbonates and fractured sandstones and carbonates under hydrostatic stress conditions were reported. Between the initial and the maximum stress levels, generally 6-8 points were taken to obtain the porosity exponent A. As shown in Table 4, porosity exponents A in unfractured sandstone cores were in the range 1.9-2.3. There is general agreement between the exponents from simulations and those from the Carman-Kozeny equation and experiments. This agreement indicates that stress sensitivity of porosity and absolute permeability of our medium is mostly similar to those of an idealized capillary tube bundle and the tight sandstones previously studied.

Table 4. Porosity exponents in real rocks from experiments of Petunin et al. [19], under hydrostatic loading condition.

Rock Type	A, range	A, average	A, median	Porosity	Permeability
Tight Sandstones	1.9-2.3	2.1	2.1	~9%	~0.04 md
Carbonates	2.7-40	11.5	10	3.9%-28.2%	0.002-5 md
Fractured cores	11-128	36	31	n/a	3.8-1150 md

Experimental data additionally indicate that values of A are higher in unfractured carbonates and fractured cores. A varied from 2.7 to 40 in unfractured carbonates and from 11 to 128 in fractured cores. High values of A in carbonates and fractured cores were attributed to their heterogeneous pore structure and dual-porosity nature [19, 20]. Pore throats or fractures that control the overall permeabilities of cores only contribute to a small fraction of the net porosity. If they are also the "weakest" parts of the net porosity that are collapsed during a compaction, a small reduction in porosity from collapsed pore throats or fractures can lead to a very high reduction in permeability, generating high values of A [21]. Take carbonates as an example: many carbonates contain vugs that contribute significantly to the overall porosity. These vugs, however, do not form a continuous flow path and permeability is controlled by much smaller pores that connect the vugs.

During a compaction, a certain fraction of porosity reduction, if occurred in the vugs, would not significantly affect permeability of the medium. If, however, this fraction of reduction occurs to the connecting pores, drastic reduction in the absolute permeability of the medium is to be expected.

To study stress sensitivity of absolute permeability in heterogeneous media, we constructed a model of a vuggy porous medium as shown in Figure 7. Within the homogeneous sphere pack, a large cylindrical tube free of particles was created along the z direction. The diameter of the tube d is 3 cm. The net porosity of this sphere pack with tube is now 0.3484 before compaction. For flows along x and y directions this cylindrical tube acts as a vug, and absolute permeabilities before compaction along these two directions, $2.18 \times 10^{-9}\, m^2$ and $2.17 \times 10^{-9}\, m^2$, were only moderately increased compared to those of the original medium ($1.52 \times 10^{-9}\, m^2$, $1.53 \times 10^{-9}\, m^2$). Permeability along the z direction, however, is dominated by the tube at $4.54 \times 10^{-6}\, m^2$. The cylindrical tube is acting like a fracture in this case. The obtained z-permeability is in excellent agreement with the analytical permeability of a medium with a single cylindrical pore: $\phi_A d^2/32 = 4.58 \times 10^{-6}$, where ϕ_A is the area fraction of the pore (0.163 in this case).

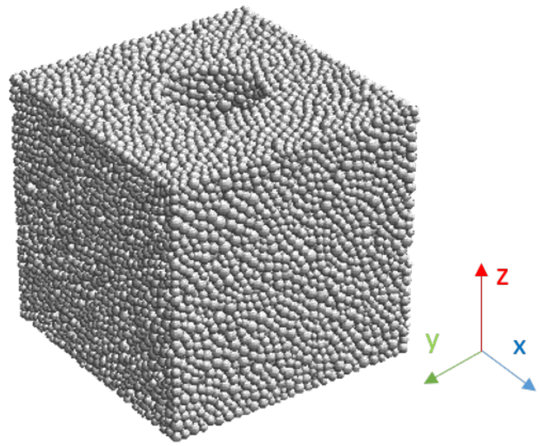

Figure 7. Heterogeneous sphere pack with a cylindrical tube in the center.

Following the same procedure for the homogeneous medium, we compacted this heterogeneous medium with tube under hydrostatic and uniaxial loading conditions using DEM and obtained changes in permeabilities using LBM. Figure 8 shows that linear relations persisted between $log_{10}(k/k_0)$ and $log_{10}(\phi/\phi_0)$ in all directions, indicating that the power-law correlation between k/k_0 and ϕ/ϕ_0 still exists. Porosity exponents A of this heterogeneous medium pack are presented in Table 5. With hydrostatic loading, along x and y directions A_x and A_y increased from 3.4~3.5 of the original medium to 4.7~4.9, indicating that permeability-controlling pores in the medium were more severely compacted. Isolated vugs therefore could indeed increase porosity exponent A. Along the z direction, A_z decreased from 3.5 to 1.9. Different from flows along x and y directions, flow and permeability along z is dominated by the cylindrical tube. At the end of compaction, pore volume of the cylinder only decreased by 1.34%. In contrast, pore volume of the entire medium decreased by 13.6%. The permeability of the medium did not decrease significantly because the volume of the cylinder did not change significantly. Thus, a lower A_z was observed. With uniaxial loading, A_x and A_y of the vuggy medium increased to 5.2 and 3.7, respectively. By comparing to those of the homogenous medium ($A_x = 3.8$, $A_y = 2.8$), we observed that the tube in the role of an isolated vug increased porosity exponent. A_z on the other hand decreased, from 3.8 to 2.3, similar to hydrostatic loading.

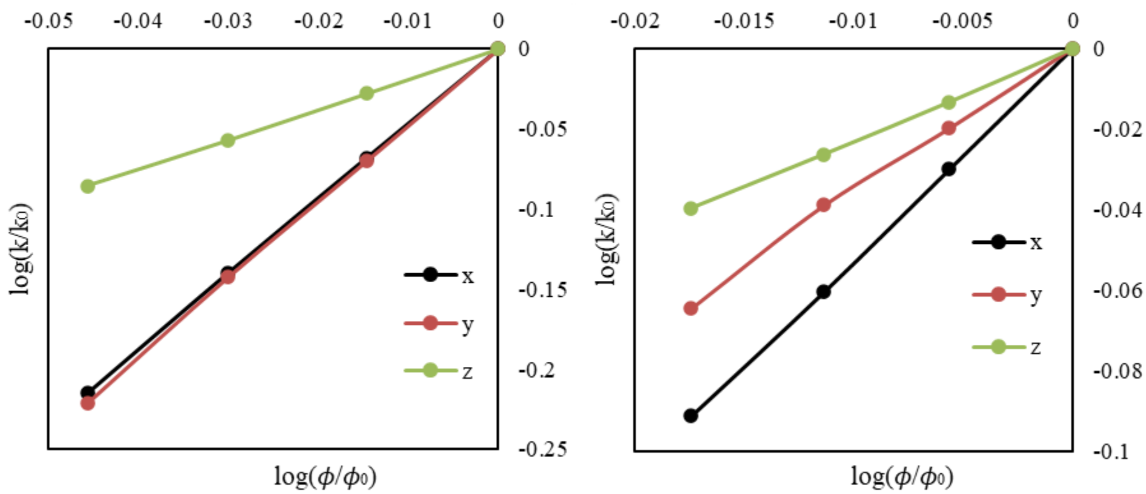

(a) (b)

Figure 8. Relations between changes of porosities and permeabilities in heterogeneous sphere pack; hydrostatic loading (a); uniaxial loading (b).

Table 5. Porosity exponents of the heterogeneous sphere pack

Hydrostatic loading			Uniaxial loading		
A_x	A_y	A_z	A_x	A_y	A_z
4.7	4.9	1.9	5.2	3.7	2.3

3.3 Relative permeability under stress

In this section, stress sensitivity of relative permeability is evaluated using a color-gradient LB model. Validation of the applied model was conducted through simulation of a layered two-phase flow in a 2D horizontal channel. The width of the channel is 2b ($-b \leq y \leq b$). The non-wetting fluid was placed in the center of the channel ($-a \leq y \leq a$) and the wetting fluid was placed near solid walls at $y = \pm b$. The channel was bounded by periodic boundaries in the x direction. A constant body force F in the x direction was applied to both fluids, leading to quadratic velocity profiles in the channel

$$u_x(y) = \begin{cases} A_1 y^2 + C_1, \ \ |y| < a \\ A_2 y^2 + B_2 y + C_2, \ \ a \leq |y| \leq b \end{cases} \tag{21}$$

In Eq. (21), $A_1 = -\frac{F}{2\mu_{nw}}$, $A_2 = -\frac{F}{2\mu_w}$, $B_2 = 2(A_1 M - A_2)a$, $C_1 = (A_2 - A_1)a^2 - B_2(b-a) - A_2 b^2$, and $C_2 = -A_2 b^2 - B_2 b$. $M = \frac{\mu_{nw}}{\mu_w}$ is the viscosity ratio of the fluids. From the velocity profiles, the relative permeabilities of the two fluids are [64]

$$k_{\mathrm{rw}} = \frac{1}{2} S_w^2 (3 - S_w) \tag{22}$$

$$k_{\mathrm{rnw}} = S_{nw}[\frac{3}{2}M + S_{nw}^2\left(1 - \frac{3}{2}M\right)] \tag{23}$$

where k_{rw} and k_{rnw} are relative permeabilities of wetting fluid and non-wetting fluid respectively, S_w and S_{nw} are the saturations of wetting fluid and non-wetting fluid respectively. The relative permeability is calculated by using the extended Darcy's law [39]. In simulation, the size of the channel was 10×100. Simulated relative permeabilities are compared with analytical solutions in Figure 9, using two viscosity ratios (M = 0.2 and 5). Our simulated relative permeabilities match well with analytical solutions for both cases.

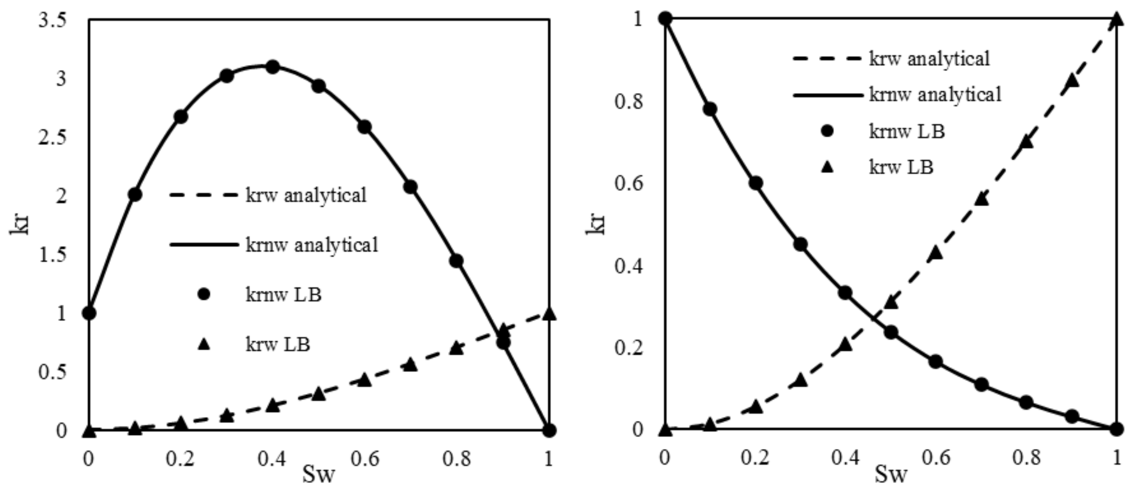

(a) (b)

Figure 9. Comparison of relative permeabilities of layered two-phase flows in a channel, (a) M = 5.0; (b) M = 0.2.

In the study of stress-dependent relative permeability, we only studied homogenous medium. To obtain a steady relative permeability for heterogeneous medium, it is required that fluids travel through pore space representative of the entire domain several times. For LB simulations of multiphase flows in porous media, we also need to keep the Mach number of the flow small to reduce compressibility error and control the capillary number. This requirement means hundreds of millions of time steps are generally needed. Though our simulator is parallelized, such a simulation in 3D is still not practical. Thus, two-phase flows through heterogeneous medium, where it is needed that fluids flow through not only the matrix of the medium but also the embedded tube, was not attempted. In two-phase flow simulations carried out for the compacted homogeneous medium, a 200^3 computational domain was taken from the center of the 400^3 domain used in single-phase flow simulations to reduce computational cost. Since the strain of the medium is relatively small and changes in relative permeability are not as significant as that in absolute permeability, only the uncompacted medium and the medium at the final stage of compaction were studied. For the homogeneous medium, the reduced domain is still a good representation of the medium because its porosity and permeability are only different from those of the larger domain by 0.2% and 3.5%, respectively. In the simulations, periodic boundary condition was applied to all sides. Saturation was established by initializing all fluid nodes probabilistically, i.e. a fluid node's probability to be assigned with the wetting fluid is S_w. After initialization, a body force of $F = 10^{-4}$ was assigned to the fluids along the direction of interest. Densities of fluids are identical. When there is a viscosity contrast, velocities of different phases are not the same, and it is not straightforward to calculate the capillary number using its common definition. In some work [64, 65], a capillary number $Ca = F/\sigma$, where σ is the interfacial tension, was used to characterize the flows. However, we found such a capillary number is not dimensionless. Instead, we defined the capillary number as $Ca = Fk_a/\sigma$, where k_a is the absolute permeability of uncompacted medium. For medium compacted by hydrostatic loading, relative permeabilities for flows along x, y, and z directions are very similar. For this reason, we will only present results obtained with F set in the x direction. For medium compacted by uniaxial loading, we found that relative permeability was not affected by compaction, when flow was aligned to the direction of compaction (y). Thus, only relative permeabilities of flows along x and z directions are presented.

On the effect of wettability, Figure 10 presents the relative permeabilities of the original sphere pack using two different contact angles: $\theta = 90°$ and $30°$. In these cases, the two fluids have equal viscosity, $\sigma = 0.0167$, and $Ca = 2.9 \times 10^{-4}$. Changing the wetting condition from neutral (90°) to preferential (30°) decreased the relative permeability of the wetting fluid and increased that of the non-wetting fluid which was also reported in previous studies [39, 66]. Figure 11 presents the stress sensitivity of these two sets of relative permeabilities under different conditions of loading. Figure 11a and Figure 11b are for hydrostatic loading and Figure 11c and Figure 11d are for uniaxial loading. These cases show that, although porosity and permeability were clearly changed by compaction, relative permeability curves were nearly not affected. It is only in the medium with preferential wettability that we found the relative permeability of the wetting phase slightly increased. This observed increase may be attributed to increased accumulation of the wetting phase near pore throats. We note that slightly increased relative permeability of the wetting phase has been found in some experimental studies [31, 33].

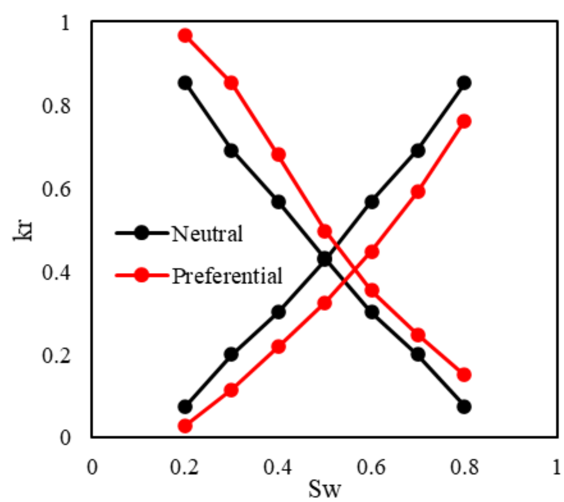

Figure 10. Effect of wettability on the relative permeability of the original medium. Black lines are at neutral wetting condition ($\theta = 90°$) and red lines are at preferential wetting condition ($\theta = 30°$).

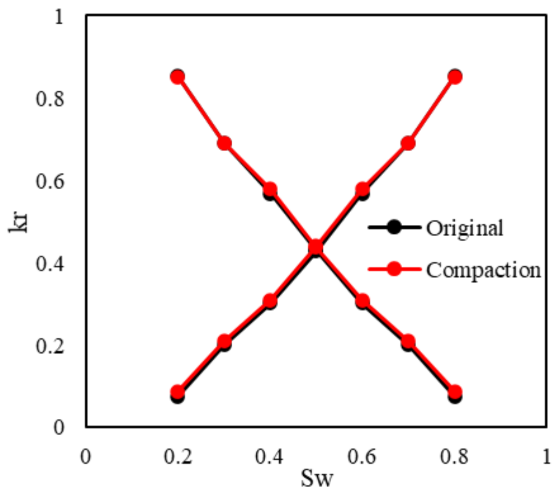

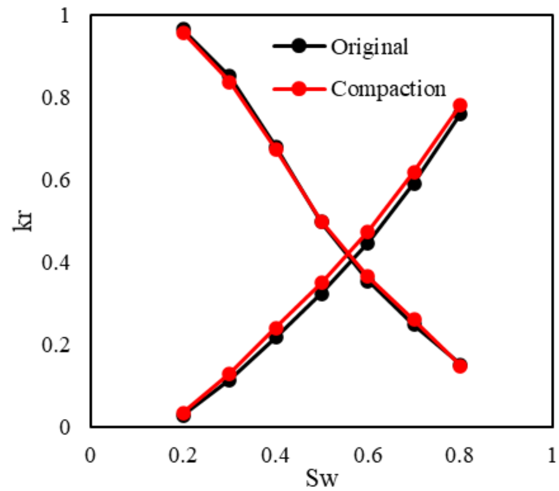

(a) (b)

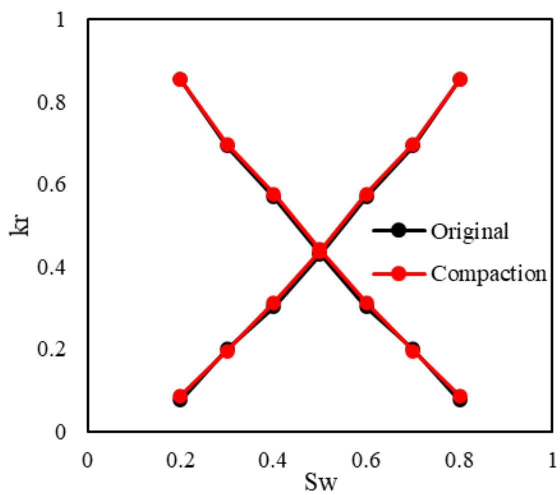

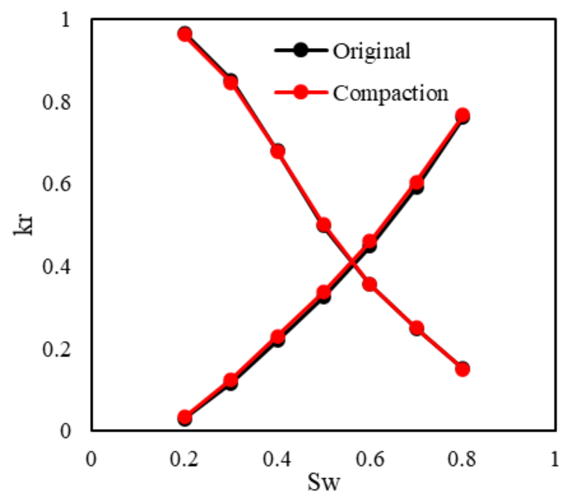

(c) (d)

Figure 11. Relative permeabilities of compacted media with neutral and preferential wettability; (a) hydrostatic loading, $\theta = 90°$; (b) hydrostatic loading, $\theta = 30°$; (c) uniaxial loading, $\theta = 90°$; (d) uniaxial loading, $\theta = 30°$.

Whereas the sole influence of wettability to relative permeability was identified to be modest, the dependence of relative permeability on viscosity ratio was found to be significant. Figure 12 presents the relative permeabilities of the uncompacted medium at three different viscosity ratios

($M = 5, 1, 0.2$). In these cases, $\theta = 30°$, $\sigma = 0.015$, and $Ca = 3.3 \times 10^{-4}$. It is observed that relative permeability of the non-wetting phase increased with increasing M, and that of the wetting phase decreased. The influence of viscosity ratio on the relative permeability was much stronger for the non-wetting phase. This is because the wetting phase occupies small pores and corners of large pores, flow of the non-wetting phase tends to occur through centers of pores and it is significantly facilitated by films of wetting phase on the solid when the non-wetting phase is the more viscous. The dependence of relative permeability on viscosity ratio is well known as the lubrication effect and has been well discussed in the literature [39, 48].

Figure 13 presents stress sensitivity of relative permeabilities of cases of the highest and the lowest M, under hydrostatic and uniaxial loading conditions. Figure 13a and Figure 13b are for hydrostatic loading and Figure 13c and Figure 13d are for uniaxial loading. We found that hydrostatic loading and uniaxial loading have similar influences over the relative permeability curves. Relative permeabilities of the wetting phase were slightly increased by compaction, regardless of viscosity ratio. Compaction affects relative permeability of the non-wetting phase more than relative permeability of the wetting phase. This is in agreement with previous experimental studies [26, 27, 30]. Moreover, relative permeabilities of the non-wetting phase were increased by compaction when $M = 5$. They, however, were decreased by compaction when $M = 0.2$. These trends were observed under both loading conditions but were clearer in the case of hydrostatic loading because of stronger compaction of pores. This is because the smaller pores and corners of pores in the medium were more easily compacted by stress, which is beneficial to the formation of thin films of wetting phase on rock surface. Thus, lubrication effect should be more significant in this compacted media, which explains the trend observed in altered relative permeability.

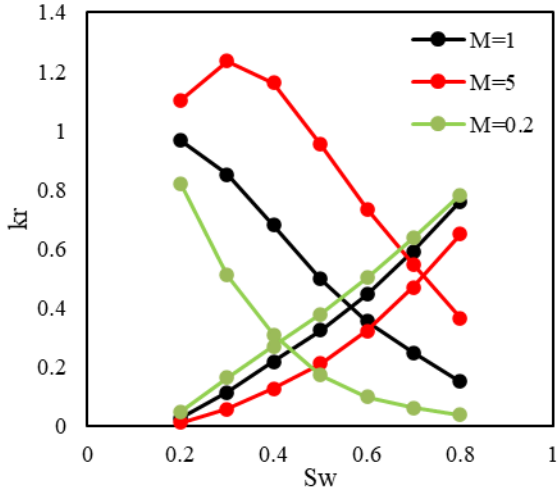

Figure 12. Effect of wettability on relative permeability in the original, uncompacted medium.

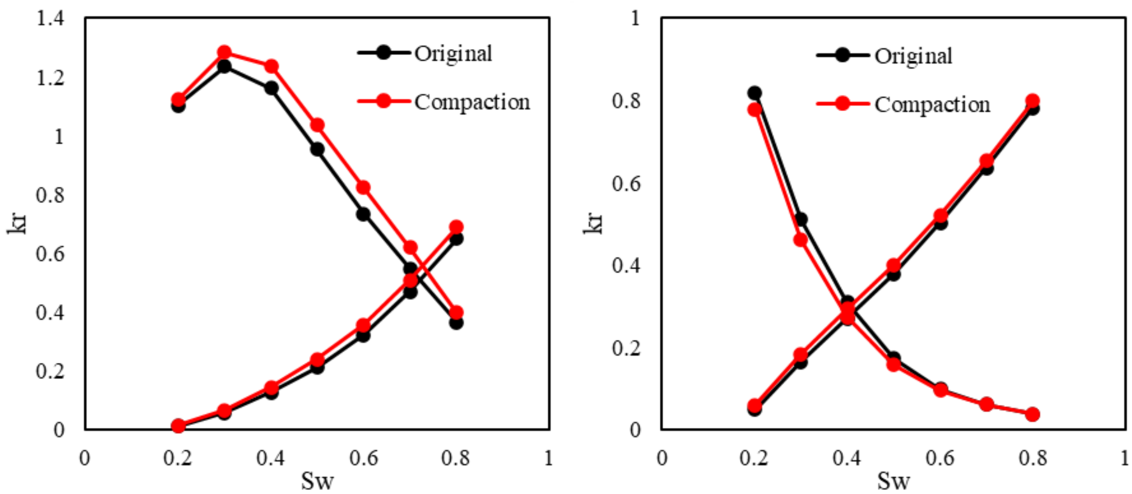

(a) (b)

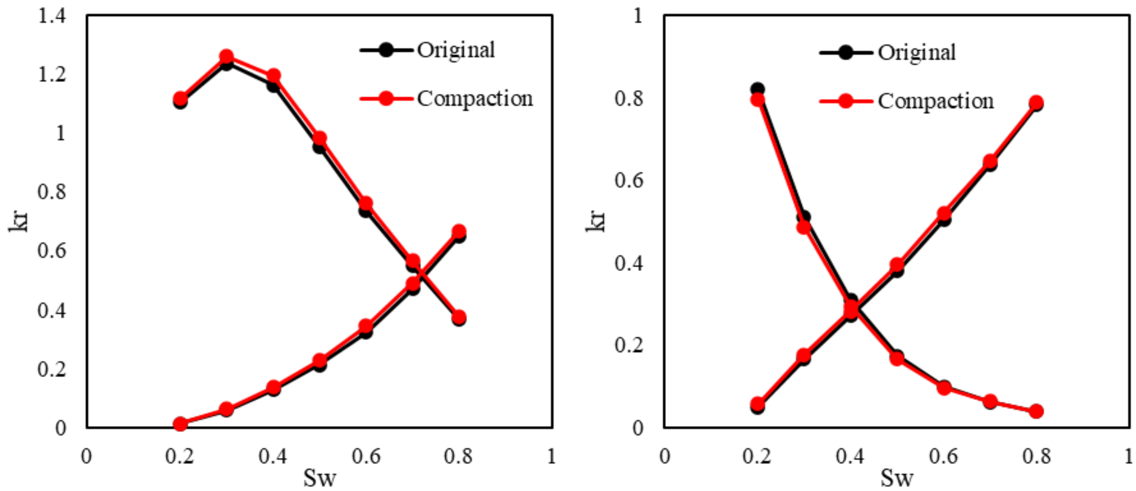

(c) (d)

Figure 13. Relative permeabilities of compacted media under (a) hydrostatic loading condition, $M = 5$; (b) hydrostatic loading condition, $M = 0.2$; (c) uniaxial loading condition, $M = 5$; (d) uniaxial loading condition, $M = 0.2$.

Two-phase flows in porous media are also strongly affected by capillary number Ca [39, 48]. Existing experiments and numerical simulations suggest that relative permeabilities of both wetting and non-wetting phases should increase with increasing Ca. In the cases that we presented thus far, Ca is 2.9×10^{-4} when $M = 1$ and 3.3×10^{-4} when $M = 0.2$ or and $M = 5$. To investigate the effect of compaction on relative permeabilities during compaction at different Ca, additional cases were conducted with $F = 10^{-3}$. The interfacial tension is $\sigma = 0.015$, leading to an increased capillary number of 3.3×10^{-3}. Contact angle was still set to $\theta = 30°$. Figure 14 presents relative permeabilities of uncompacted medium at two different capillary numbers, 3.3×10^{-4} (low) and 3.3×10^{-3} (high), for viscosity ratios of 0.2 and 5. It is known that when Ca is higher, effect of viscous force is stronger relative to capillary force, and this helps both wetting and non-wetting phases overcome capillary resistance and flow. The observed trend that relative permeabilities of both wetting and non-wetting phases increased with increasing *Ca* is reasonable.

In Figure 15 we compared relative permeability curves of original and compacted media at a higher capillary number. We found that compaction increased relative permeabilities of the wetting phase when the loading is hydrostatic, as shown in Figure 15a and 15b. When the loading is uniaxial, relative permeabilities of the wetting phase also increased with compaction, but changes were small and not clearly visible in Figure 15c and 15d. Changes in the relative permeabilities of the non-wetting phase are more complex. Figure 15a and Figure 15b show that, for hydrostatic loading and when $M = 5$, with compaction relative permeability of the non-wetting phase slightly increased. Compared to Figure 13a, there is no qualitative change in the trend, but the effect of compaction was *less* at the higher capillary number. When $M = 0.2$, with compaction relative permeability of the non-wetting phase decreased. Compared to Figure 13b, the trend is the same, but compaction reduced relative permeability of the non-wetting phase *more* when *Ca* is high. When *Ca* is low, the stronger capillary force is beneficial for the accumulation of the non-wetting phase in the middle of pores, and this accentuate the effect of wetting fluid film on the mobility of the non-wetting phase through lubrication. The results from uniaxial loading are presented in Figure 15c and Figure 15d. Compared to hydrostatic loading, similar behaviors of relative permeability were observed, but all with lesser magnitudes.

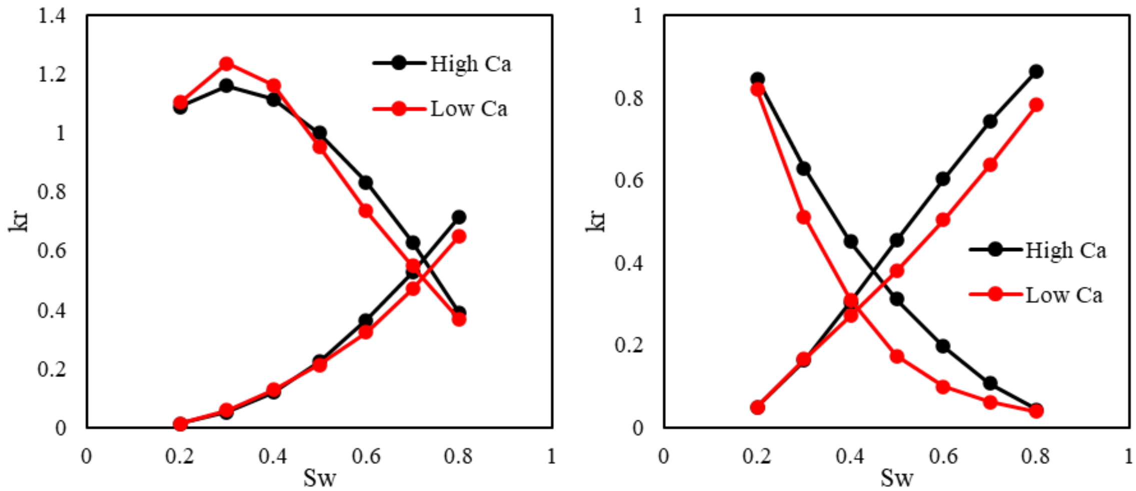

(a) (b)

Figure 14. Effect of capillary number on the relative permeability of original sphere pack; (a) $M = 5$; (b) $M = 0.2$.

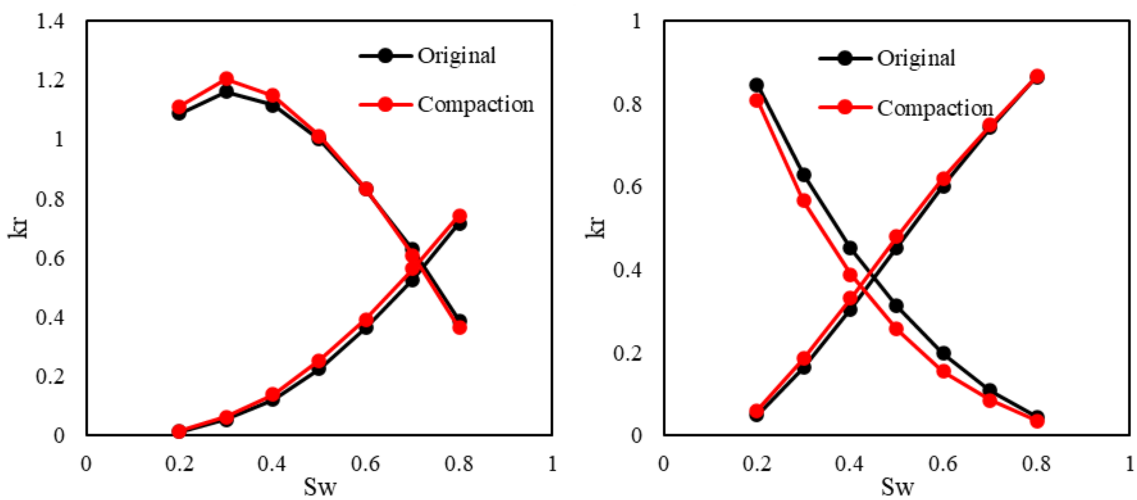

(a) (b)

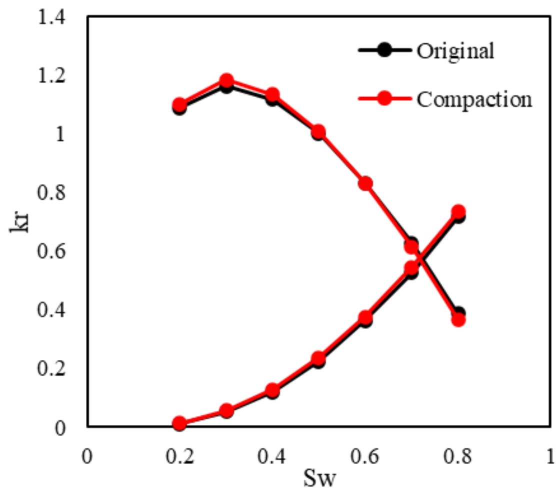

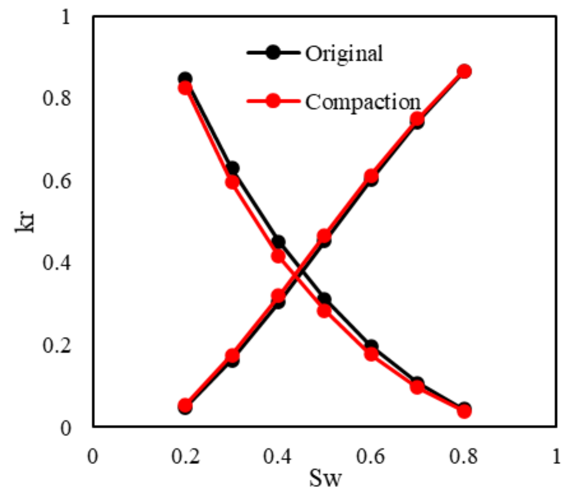

(c) (d)

Figure 15. The relative permeabilities of compacted media with $Ca = 3.3 \times 10^{-3}$, under (a) hydrostatic loading condition, $M = 5$; (b) hydrostatic loading condition, $M = 0.2$; (c) uniaxial loading condition, $M = 5$; (d) uniaxial loading condition, $M = 0.2$.

4. Conclusions

In this work, we studied stress-dependent absolute and relative permeabilities in porous media packed by spherical particles. Compaction of porous media was modeled using a discrete element method. Three stages of strain were simulated for both hydrostatic loading and uniaxial loading. Absolute and relative permeabilities before and after compaction were simulated using lattice Boltzmann methods.

In the homogeneous packing, absolute permeability decreased linearly with strain under the hydrostatic loading condition and slightly nonlinearly under the uniaxial loading condition. Uniaxial loading generated anisotropy in the absolute permeability and those along lateral directions were more sensitive to change of porosity. In all cases, changed porosity and absolute permeability during compaction follow a power-law relation. The porosity exponent of homogeneous packing is close to the theoretical value from the Carman-Kozeny equation and experimental value of sandstones.

To study the effect of heterogeneity, a vuggy porous medium was built by creating a cylindrical tube in the middle of homogeneous pack. Insertion of this tube increased porosity exponent along the directions perpendicular to the tube. When flows are perpendicular to the cylindrical tube, the tube acts as a vug. During compactions, the permeability-controlling pores in the matrix of the medium were more severely compacted, leading to high porosity exponents. In the direction aligned with the tube, the diameter of the tube controls the permeability. The tube's deformation was less than that of the surrounding matrix. For this reason, a lower porosity exponent was observed in the direction aligned with the tube.

Stress-dependent relative permeability was studied at different viscosity ratios, wettability conditions, and capillary numbers. It was found that relative permeability only changes with stress when fluids demonstrate preferential wetting. Relative permeability of the wetting phase (k_{rw}) was often increased slightly by compaction, due to accumulation of wetting phase in smaller pores and formation of continuous pathways. Relative permeability of the non-wetting phase (k_{rnw}), on the other hand, was more significantly affected by compaction. Due to more significant lubrication effect from the wetting fluid in compacted media, k_{rnw} was increased by compaction when the non-wetting phase is the more viscous but decreased when the non-wetting phase is the less viscous phase. The degree in which compaction affects relative permeability of the non-wetting phase was found to be dependent on the capillary number. Simulations with lower capillary numbers exhibited more stress dependent relative permeability of the non-wetting phase. We believe that this is due to the stronger preference for the non-wetting phase to favor centers of pores at lower capillary numbers, which accentuated the lubrication effects.

Finally, though we only focused on sphere pack, knowledge learned from this theoretical study could be applied to more complex media. At the same time, we are also aware that there are still gaps when one translates results from sphere packs to real rocks. Complex pore structure, distribution of pore size and kerogen types [67] in real rock may pose a challenge.

Acknowledgment

J.H. gratefully acknowledges the High Performance Research Computing Facilities in Texas A&M University. X.Y. acknowledges computational resource at the Colorado School of Mines provided by the Golden Energy Computing Organization. J.S. would like to acknowledge support from EPSRC EP/N025318/1, The Royal Academy of Engineering/The Leverhulme Trust Senior Research Fellowship LTSRF1617/13/2 and NERC NE/T010517/1 and NE/R011001/1.

Reference

[1] Corapcioglu, M.Y. and Brutsaert, W., 1977. Viscoelastic aquifer model applied to subsidence due to pumping. Water Resour. Res. 13(3): 597-604. https://doi.org/10.1029/WR013i003p00597.

[2] Gambolati, G., and Teatini, P., 2015. Geomechanics of subsurface water withdrawal and injection. Water Resour. Res. 51(6): 3922-3955.

[3] Davies, J.P., and Davies, D.K. 2001. Stress-Dependent Permeability: Characterization and Modeling. SPE journal 6(2): 224-235. https://doi.org/10.2118/71750-PA.

[4] Huang, J., Jin, T., Chai, Z. et al. 2019. Compositional simulation of fractured shale reservoir with distribution of nanopores using coupled multi-porosity and EDFM method. Journal of

Petroleum Science and Engineering 179: 1078-1089. https://doi.org/10.1016/j.petrol.2019.05.012.

[5] Kim, T.H., Cho, J., and Lee. K.S., 2017. Evaluation of CO2 injection in shale gas reservoirs with multi-component transport and geomechanical effects. Applied Energy 190: 1195-1206. https://doi.org/10.1016/j.apenergy.2017.01.047.

[6] Huang, J., Jin, T., Barrufet, M. et al. 2020. Evaluation of CO2 injection into shale gas reservoirs considering dispersed distribution of kerogen. Applied Energy 260, 114285. https://doi.org/10.1016/j.apenergy.2019.114285.

[7] Jin, L., Hawthorne, S., Sorensen, J., 2017. Advancing CO2 enhanced oil recovery and storage in unconventional oil play—experimental studies on Bakken shale. Applied Energy 208: 171-183. https://doi.org/10.1016/j.apenergy.2017.10.054.

[8] Du, F., Huang, J., Chai, Z. et al. 2020. Effect of vertical heterogeneity and nano-confinement on the recovery performance of oil-rich shale reservoir, Fuel 267, 117199. https://doi.org/10.1016/j.fuel.2020.117199.

[9] Okazaki, K., Noda, H., Uehara, S., et al. 2014. Permeability, porosity and pore geometry evolution during compaction of Neogene sedimentary rocks. Journal of Structural Geology 62: 1-12. https://doi.org/10.1016/j.jsg.2013.12.010.

[10] Bhandari, A.R., Flemings, P.B., Polit, P.J. 2015. Anisotropy and Stress Dependence of Permeability in the Barnett Shale. Transport in Porous Media volume 108: 393–411. http://dx.doi.org/10.1007/s11242-015-0501-1.

[11] He, J. Chen S.H., and Shahrour, I. 2013. Numerical estimation and prediction of stress dependent permeability tensor for fractured rock masses. International Journal of Rock Mechanics and Mining Sciences 59: 70-79. https://doi.org/10.1016/j.ijrmms.2012.12.001.

[12] Worthington, P.F., 2008. A diagnostic approach to quantifying the stress sensitivity of permeability. Journal of Petroleum Science and Engineering 61: 49-57. https://doi.org/10.1016/j.petrol.2008.03.003.

[13] Tan X.H., Li, X.P., Liu, J.Y., et al. 2015. Study of the effects of stress sensitivity on the permeability and porosity of fractal porous media. Physics Letters A 379(39): 2458-2465. https://doi.org/10.1016/j.physleta.2015.06.025.

[14] Bakhshian, S. and Sahimi M. 2016. Computer simulation of the effect of deformation on the morphology and flow properties of porous media. PHYSICAL REVIEW E 94, 042903. https://doi.org/10.1103/PhysRevE.94.042903.

[15] Bernabé, Y. 1991. Pore Geometry and Pressure Dependence of the Transport Properties in Sandstone. Geophysics, 56(4): 436-446. https://doi.org/10.1190/1.1443061.

[16] Doyen, P. M. 1988. Permeability, Conductivity, and Pore Geometry of Sandstone. J. Geophys. Res. Solid 93, 7729-7740. https://doi.org/10.1029/JB093iB07p07729.

[17] David, C., Wong, T. F., Zhu, W. et al. 1994. Laboratory measurement of compaction induced permeability change in porous rocks: Implications for the generation and maintenence of pore pressure excess in the crust. Pure Appl. Geophy. 143: 425-456. https://doi.org/10.1007/BF00874337.

[18] Dong, J. J., Hsu, J. Y., Wu, W. et al. 2010. Stress-dependence of the permeability and porosity of sandstone and shale from TCDP Hola-A. Int. J. Rock Mech. Min. 47(7): 1141-1157. https://doi.org/10.1016/j.ijrmms.2010.06.019.

[19] Petunin, V.V., Yin, X., and Tutuncu, A.N., 2011. Porosity and Permeability Changes in Sandstones and Carbonates Under Stress and Their Correlation to Rock Texture. Paper

presented at Canadian Unconventional Resources Conference, 15-17 November, Calgary, Alberta, Canada. https://doi.org/10.2118/147401-MS.

[20] Petunin, V.V., Labra, C., Xiao, F., et al. 2013. Porosity and Permeability Change under Stress and Correlation to Rock Texture. Paper presented at Fifth Biot Conference on Poromechanics July 10-12, 2013, Vienna, Austria. https://doi.org/10.1061/9780784412992.124.

[21] Bernabé, Y., Mok, U., and Evans, B. 2003. Permeability-porosity Relationships in Rocks Subjected to Various Evolution Processes. Pure and applied geophysics, 160: 937–960. https://doi.org/10.1007/PL00012574

[22] Fatt I. 1953. The Effect of Overburden Pressure on Relative Permeability. J. Pet. Technol. 5, 15-16. https://doi.org/10.2118/953325-G.

[23] Thomas, R.D., and Ward, D.C., 1972. Effect of Overburden Pressure and Water Saturation on Gas Permeability of Tight Sandstone Cores. J. Pet. Technol. 24: 120-124. https://doi.org/10.2118/3634-PA.

[24] Zhang, X., Wu, C., and Liu, S., 2017. Characteristic analysis and fractal model of the gas-water relative permeability of coal under different confining pressures. J. Pet. Sci. Eng. 159: 488–496. https://doi.org/10.1016/j.petrol.2017.09.057.

[25] Haghi, A.H., Chalaturnyk, R. and Talman, S. 2019. Stress-Dependent Pore Deformation effects on Multiphase Flow Properties of Porous Media. Scientific Reports 9, 15004. https://doi.org/10.1038/s41598-019-51263-0.

[26] Ali H., Al-Marhoun, M. and Abu-Khamsin S., 1987. The Effect of Overburden Pressure on Relative Permeability. Paper presented at Middle East Oil Show, 7-10 March, Bahrain, SPE-15730-MS. https://doi.org/10.2118/15730-MS.

[27] Jones, C., Al-Quraishi, A., Somerville J.M. et al. 2001. Stress Sensitivity of Saturation and End-point Relative Permeabilities. Paper presented at International Symposium of the Society of Core Analysts - Edinburgh, United Kingdom.

[28] Al-Quraishi, A. and Khairy, M. 2005. Pore pressure versus confining pressure and their effect on oil–water relative permeability curves. Journal of Petroleum Science and Engineering 48: 120-126. https://doi.org/10.1016/j.petrol.2005.04.006.

[29] Gawish, A. and Al-Homadhi E. 2008. Relative permeability curves for high pressure, high temperature reservoir conditions. Oil Gas Business.

[30] Adenutsi, C.D., Li Z., Xu Z. et al. 2019. Influence of net confining stress on NMR T2 distribution and two-phase relative permeability. Journal of Petroleum Science and Engineering 178: 766-777. https://doi.org/10.1016/j.petrol.2019.03.083.

[31] Wilson, J., 1956. Determination of relative permeability under simulated reservoir conditions. AIChE J. 2: 94–100. https://doi.org/10.1002/aic.690020120.

[32] Hamoud, M., Chalaturnyk, R., Leung, J. 2012. Influence of Geomechanical Processes on Relative Permeability. Canadian Rock Mechanics Symposium, Edmonton, Alberta, 9 p.

[33] Al-Quraish, A., Almisned, O.A., and Al-Awad M.N.J. 2010. Relative Permeabilities of Homogeneous and Heterogeneous Laminated Rock Samples under Hydrostatic and Triaxial Stresses. J. King Saud Univ. Eng. Sci. 22(2): 101-110. https://doi.org/10.1016/S1018-3639(18)30497-5.

[34] Fagbemi, S., Tahmasebi P., and Piri, M. 2018. Pore-scale modeling of multiphase flow through porous media under triaxial stress. Advances in Water Resources, 122: 206-216. https://doi.org/10.1016/j.advwatres.2018.10.018.

[35] Fagbemi, S., Tahmasebi P., and Piri, M. 2020. Numerical modeling of strongly coupled microscale multiphase flow and solid deformation. Int J Numer Anal Methods Geomech 44(2): 161-182. https://doi.org/10.1002/nag.2999.

[36] Fan, M., McClure, J., Han, Y. et al. 2018. Interaction Between Proppant Compaction and Single-/Multiphase Flows in a Hydraulic Fracture. SPE Journal 23 (04), 1290-1303. https://doi.org/10.2118/189985-PA.

[37] Owens, W. W. and Archer, D. L., 1971. The effect of rock wettability on oil-water relative permeability relationships, J. Pet. Tech. 23, 873–878. https://doi.org/10.2118/3034-PA.

[38] Avraam D.G. and Payatakes A.C. 1995. Flow regimes and relative permeabilities during steady-state two-phase flow in porous media. Journal of Fluid Mechanics. 293: 207-236. https://doi.org/10.1017/S0022112095001698.

[39] Li, H., Pan, C., and Miller, C.T., 2005. Pore-scale investigation of viscous coupling effects for two-phase flow in porous media. Phys. Rev. E 72, 026705. https://doi.org/10.1103/PhysRevE.72.026705.

[40] Ramstad, T., Idowu, N., Nardi, C., et al. 2012. Relative Permeability Calculations from Two-Phase Flow Simulations Directly on Digital Images of Porous Rocks. Transport in Porous Media 94: 487–504. https://doi.org/10.1007/s11242-011-9877-8.

[41] Gunstensen, A.K., Rothman, D.H., Zaleski, S., et al. 1991. Lattice Boltzmann model of immiscible fluids. Physical Review A 43, 4320. https://doi.org/10.1103/PhysRevA.43.4320.

[42] Liu, H., Valocchi, A.J. and Kang, Q., 2012. Three-dimensional lattice Boltzmann model for immiscible two-phase flow simulations. Phys. Rev E 85, 046309. https://doi.org/10.1103/PhysRevE.85.046309.

[43] Ba, Y., Liu, H., Li, Q., et al. 2016. Multiple-relaxation-time color-gradient lattice Boltzmann model for simulating two-phase flows with high density ratio. Phys. Rev E 94, 023310. https://doi.org/10.1103/PhysRevE.94.023310.

[44] Shan, X., and Chen, H., 1993. Lattice Boltzmann model for simulating flows with multiple phases and components. Physical Review E 47, 1815. https://doi.org/10.1103/PhysRevE.47.1815.

[45] Shan, X., and Doolen, G., 1995. Multicomponent lattice-Boltzmann model with interparticle interaction. Journal of Statistical Physics 81: 379-393. https://doi.org/10.1007/BF02179985.

[46] Swift, M.R., Osborn, W.R., and Yeomans, J.M., 1995. Lattice Boltzmann simulation of nonideal fluids. Physical Review Letters 75, 830. https://doi.org/10.1103/PhysRevLett.75.830.

[47] He, X., Chen, S., and Zhang, R. 1999. A Lattice Boltzmann Scheme for Incompressible Multiphase Flow and Its Application in Simulation of Rayleigh–Taylor Instability, J. Comput. Phys. 152(2): 642-663. https://doi.org/10.1006/jcph.1999.6257.

[48] Huang, J., Xiao, F., and Yin, X., 2017. Lattice Boltzmann simulation of pressure-driven two-phase flows in capillary tube and porous medium. Computers and Fluids 155: 134-145. https://doi.org/10.1016/j.compfluid.2017.05.027.

[49] Zhao, J., Kang, Q., Yao, J., et al. 2018. The effect of wettability heterogeneity on relative permeability of two-phase flow in porous media: A lattice Boltzmann study. Water Resources Research, 54, 1295–1311. https://doi.org/10.1002/2017WR021443.

[50] Jiang, F., and Tsuji, T. 2016. Estimation of three-phase relative permeability by simulating fluid dynamics directly on rock-microstructure images. Water Resour. Res. 53: 11–32, https://doi:10.1002/2016WR01909.

[51] Potyondy, D. O. and Cundall, P. A. 2004. A bonded-particle model for rock. Int. J. Rock Mech. Min. 41: 1329–1364. https://doi.org/10.1016/j.ijrmms.2004.09.011.

[52] Boutt, D.F. and McPherson B.J.O.L. 2002. Simulation of sedimentary rock deformation: Lab-scale model calibration and parameterization. Geophysical research Letters 29(4), 1054. https://doi.org/10.1029/2001GL013987.

[53] Powell and McBride 2006. What is required from DEM simulations to model breakage in mills? Minerals Engineering 19(10): 1013-1021. https://doi.org/10.1016/j.mineng.2006.03.009.

[54] Labra, C., 2012. Advances in the development of the discrete element method for excavation processes. PhD thesis. Universitat Politècnica de Catalunya.

[55] Jauffrès, D., Martin, C.L., Lichtner, A. et al. 2012. Simulation of the elastic properties of porous ceramics with realistic microstructure. Modelling Simul. Mater. Sci. Eng. 20 045009. https://doi.org/10.1088/0965-0393/20/4/045009.

[56] Rojek, J., Labra, C., Su, O., et al. 2012. Comparative study of different discrete element models and evaluation of equivalent micromechanical parameters. International Journal of Solids and Structures 49(13): 1497-1517. https://doi.org/10.1016/j.ijsolstr.2012.02.032.

[57] Xiao, F, and Yin, X., 2016. Geometry models of porous media based on Voronoi tessellations and their porosity–permeability relations. Computers & Mathematics with Applications 72(2): 328-348. https://doi.org/10.1016/j.camwa.2015.09.009.

[58] Sukop, M.C. and Thorne, D.T., 2007. Lattice Boltzmann Modeling: An Introduction for Geoscientists and Engineers. Springer. https://doi.org/10.1007/978-3-540-27982-2.

[59] Lallemand, P., and Luo, L.-S., 2000. Theory of the lattice Boltzmann method: Dispersion, dissipation, isotropy, Galilean invariance, and stability. Physical review. E, Statistical Physics,

Plasmas, Fluids, and Related Interdisciplinary Topics. 2000 Jun;61(6 Pt A):6546-6562. https://doi.org/10.1103/physreve.61.6546.

[60] d'Humières, D., 2002. Multiple–relaxation–time lattice Boltzmann models in three dimensions. Philosophical Transactions of the Royal Society of London. Series A: Mathematical, Physical and Engineering Sciences 360, 437-451. https://doi.org/10.1098/rsta.2001.0955.

[61] Frisch, U., d'Humières, D., Hasslacher, B., et al. 1987. Lattice gas hydrodynamics in two and three dimensions. AIP Conf. Proc. Complex Systems 1: 649-707.

[62] Zhang, L., Kang, Q., Yao, J., et al. 2015. Pore scale simulation of liquid and gas two phase flow based on digital core technology. Science China technological science 58: 1375-1384. https://doi.org/10.1007/s11431-015-5842-z.

[63] Labra, C. and Oñate, E., 2009. High-density sphere packing for discrete element method simulations. Commun. Numer. Meth. En. 25, 837-849. https://doi.org/10.1002/cnm.1193.

[64] Yiotis, A.G., Psihogios, J., Kainourgiakis, M.E., et al. 2007. A lattice Boltzmann study of viscous coupling effects in immiscible two-phase flow in porous media. Colloids and Surfaces A: Physicochemical and Engineering Aspects, 300(1): 35–49. https://doi.org/10.1016/j.colsurfa.2006.12.045.

[65] Huang, H., Lu, X-y. 2009. Relative permeabilities and coupling effects in steady-state gas-liquid flow in porous media: A lattice Boltzmann study. Physics of Fluids, 21(9), 092104. https://doi.org/10.1063/1.3225144.

[66] Anderson, W. G. 1987. Wettability literature survey part 5: The effects of wettability on relative permeability. Journal of Petroleum Technology, 39(11): 1453–1468. https://doi.org/10.2118/16323-PA.

[67] Sun, Z., Li, X., Liu, W., Zhang, T., He, M. and Nasrabadi, H., 2020. Molecular Dynamics of Methane Flow Behavior through Realistic Organic Nanopores under Geologic Shale Condition: Pore size and Kerogen Types. Chemical Engineering Journal, 398, 124341.